Inorganic Chemistry

Article

pubs.acs.org/IC

Hydrothermal Fabrication of $MnCO_3$@rGO Composite as an Anode Material for High-Performance Lithium Ion Batteries

Liankai Zhou,[†,‡] Xianghua Kong,*[,†] Min Gao,[§] Fang Lian,[§] Baojun Li,[‡,∥] Zhongfu Zhou,[⊥] and Huaqiang Cao*[,‡]

[†]Institute for Advanced Materials and Technology, University of Science & Technology Beijing, Beijing 100083, People's Republic of China

[‡]Department of Chemistry, Tsinghua University, Beijing 100084, People's Republic of China

[§]School of Materials Science and Engineering, University of Science & Technology Beijing, Beijing 100083, People's Republic of China

[∥]College of Chemistry and Molecular Engineering, Zhengzhou University, Zhengzhou 450001, People's Republic of China

[⊥]Shanghai Key Laboratory for Modern Metallurgy and Materials Processing, Shanghai University, Shanghai 200072, People's Republic of China

Supporting Information

ABSTRACT: The layer structure of graphene or reduced graphene oxide (rGO) opens an avenue for the development of advanced functional materials. In this paper, a $MnCO_3$@rGO composite (MGC) was fabricated by anchoring $MnCO_3$ nanoparticles (NPs) on rGO sheets in the hydrothermal reduction process of graphene oxide by using $NaBH_4$. $MnCO_3$ NPs with an average diameter of 8–20 nm were anchored onto the surface of rGO. The layer structure of rGO was maintained in MGC. The MGC was employed as an anode active material for lithium ion batteries. Excellent performances were obtained with a high specific capacity up to 857 mA·h·g^{-1} after 100 cycles. The various charging–discharging current rates of 0.2–5.0 C exhibited no clear negative effect on the recycling stability of the MGC. The enhanced structure stability and ion and electron conductivity of the MGC are responsible for the superior electrochemical properties.

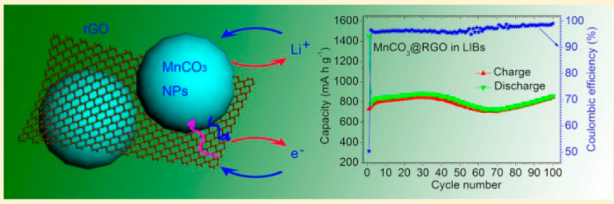

1. INTRODUCTION

Lithium ion batteries (LIBs) are of great importance for the development of electric vehicles supplemented with supercapacitors.[1] Excellent recyclability, high energy, and high power density are the main aims that will accelerate the application of LIBs in practice.[2] The research on anode materials provides a fundamental route for high-performance LIBs. There are a large amount of alloy and metal compound materials with which higher energy density compared with the current commercial anode material, graphite (372 mA·h·g^{-1}), can be obtained.[3] The main problems for these anode materials are low power density and slow charging–discharging processes, which limit the motive force, running speed, and recovery time of electric vehicles.[4,5] Another key requirement is the excellent recyclability of LIBs, based on the view of economic efficiency.[6] It is necessary to improve the electron conductivity, ion mobility, and structure stability in the charging–discharging processes for LIBs to solve these problems.[7]

Graphene and reduced graphene oxide (rGO) composed of sp^2 hybrid carbon atoms possess network structure and sheet shape in microscale with very high surface area (2680 m^2·g^{-1}) and electron conductivity.[8] The excellent chemical stability is also a feature of graphene and rGO. Inorganic nanoscaled structures will increase the surface area of the electrode, shorten the diffusion distance for lithium ions, and improve the accessibility of the active surface. Fabrication of hybrids by combining graphene or rGO with inorganic nanoparticles (NPs) should become an effective method to obtain superior anode materials for high-performance LIBs.[9−11]

Manganese is a low-cost element with large storage in the earth, and its compounds have potential applications in high-performance LIBs. Manganese oxides have been demonstrated as anode materials for LIBs. However, it is required to carry out a calcination treatment in the preparation process of manganese oxides, which increases the operation cost and danger. $MnCO_3$ will not require a high-temperature treatment for its industrial production. The high theoretic Li-storage capacity of $MnCO_3$ highlights its application prospects for LIBs. However, the low electron conductivity of $MnCO_3$ will limit its application, which can be improved by incorporating $MnCO_3$ with graphene or rGO nanosheets, which have high electron conductivity.

In this paper, a $MnCO_3$@rGO (MGC) hybrid was fabricated by *in situ* synthesis of $MnCO_3$ NPs in the hydrothermal reduction process of GO to rGOs. $MnCO_3$ NPs were anchored onto the surface of rGO nanosheets. No calcination treatment

Received: June 6, 2014
Published: August 21, 2014

is required in this solution-process preparation. The layer structure of rGO was maintained in the MGC. As an anode active material for LIBs, superior performance of the MGC, including capacity, recycling stability, and rate charging, was obtained due to its high structural stability, high electron conductivity, and large ion mobility.

2. EXPERIMENTAL SECTION

2.1. Preparation of Material. Graphite oxide was synthesized using a modified Hummer's method from graphite powders (chemically pure, CP, Sinopharm Chemical Reagent Co., Ltd.) with $NaNO_3$ (analytical reagent AR, Beijing Yili Fing Chemical Co., Ltd.), H_2SO_4 (AR, Beijing Chemical Works), and $KMnO_4$ (AR, Beijing Chemical Works), as described elsewhere.[7,11] A suspension (25 mL) of GO (30 mg) was stirred for 10 min and then ultrasonically treated for 2 h, followed by adding an aqueous solution (5 mL) of $MnCl_2 \cdot 4H_2O$ (AR, Beijing Chemical Works, 1.2 mmol). The mixture was stirred for 10 h to complete the ion exchange. Then, an aqueous solution (5 mL) of L-lysine (AR, Beijing Kebio Bio-Technique Co., Ltd., 6 mmol) was added dropwise into the above mixture with stirring for a further 10 min. An aqueous solution (5 mL) of $NaBH_4$ (AR, Tianjin Fuchen Chemical Reagents Factory, 10 mg) was added to the above suspension under stirring for 5 min. Then the mixture was transferred into an autoclave (50 mL), heated to 170 °C, and maintained at this temperature for 20 h. The resulting black solid was collected and washed with deionized water and ethanol three times, respectively. After drying at 80 °C for 5 h, the MGC was obtained.

2.2. Characterization. Fourier transform infrared (FT-IR) spectrum measurements were carried out on a Nicolet 560 Fourier transform infrared spectrophotometer. The Raman spectrum was recorded on a Renishaw RM-2000 with excitation from the 514 nm line of an Ar-ion laser with a power of about 5 mW with a resolution of 1 cm^{-1}. The phase structures of as-prepared products were characterized with X-ray diffraction (XRD, Bruker D8 advance) with Cu Kα $\lambda = 1.5406$ Å) radiation. The average crystallite size of $MnCO_3$ was estimated using the Scherrer formula:

$$D = \lambda/(\beta_{(hkl)} \cos \theta)$$

D, λ, $\beta_{(\mathrm{hkl})}$, and θ represent the diameter of the crystal particle, the wavelength of the Cu Kα source used (1.5406 Å), the full width at half-maximum (fwhm), and the Bragg angle, respectively.

X-ray photoelectron spectra (XPS) were recorded on a 250XI X-ray photoelectron spectrometer with an Al Kα and Mg/Al excitation source, where binding energies were calibrated by referencing the C 1s peak (284.8 eV) to reduce the sample charge effect.

Nitrogen adsorption−desorption isotherms were recorded at 77 K on Micromeritics TriStar 3020 II equipment.

The morphology of as-prepared products was studied by using a transmission electron microscope (TEM, Hitachi H7650B, operating at 120 kV) and high resolution TEM (HRTEM, JEOL JEM-2010F electron microscope, operating at 200 kV).

For atom force microscopy (AFM) measurement, the samples were coated on a Si surface, and AFM studies were performed using a Digital Instruments Dimension 3100 microscope in the tapping mode.

Cyclic voltammetry (CV) measurements were conducted on an electrochemistry workstation (CHI660E). The electrochemical impedance spectroscopy (EIS) measurements were also performed over a frequency range from 10^5 to 10^{-2} Hz at the amplitude of the sinusoidal voltage of 5 mV and room temperature (RT) on the same electrochemistry workstation.

Lithium ion battery performance was determined using CR 2032 type coin cells assembled in an argon-filled glovebox (MBraun). The working electrodes prepared by mixing the MGC, carbon black, and poly(vinylidene fluoride) (PVDF) at a weight ratio of 75:15:10 were pasted on pure Cu foil (15 μm) for a film (125 μm). Celgard 2400 was used as a separator. Lithium foil was used as the counter electrode. The electrolyte consisted of a solution of $LiPF_6$ (1 M) containing ethylene carbonate/dimethyl carbonate/diethyl carbonate (1:1:1, volume ratio). A galvanostatic cycling test of the assembled cells was carried out on a LAND CT2001A system in the voltage range 0.001−3.0 V (vs Li^+/Li) at various current densities (1.0 C = 600 mA·g^{-1}). The weight of the MGC in the working electrode was used to estimate the specific capacity, which was expressed in mA·h·g^{-1} of the MGC. The corresponding electrochemical behavior of commercial $MnCO_3$ (Figure S1) was also measured under the same conditions as that of MGC, compared with the MGC.

3. RESULTS AND DISCUSSION

The synthesis route of the MGC was illustrated in Scheme 1. Under hydrothermal conditions, L-lysine performed a decarboxylation process. The resulting carbonate ions reacted with Mn^{2+} and generated $MnCO_3$ NPs on the surface of GO sheets, while GO sheets were synchronously reduced to rGO by $NaBH_4$ in this process. The existence of GO reduced the size of $MnCO_3$ particles and assisted the formation of $MnCO_3$ NPs. In the absence of GO, $MnCO_3$ particles were obtained with a small Mn_3O_4 impurity through a similar hydrothermal process (Figure S2). The TEM image (Figure S3) of the as-synthesized so-called $MnCO_3$ presents particle- and rod-type shapes that are larger than the size of the $MnCO_3$ particles anchored on the rGO in the MGC. This result demonstrated that adding GO in the reaction system can help to reduce the size of the $MnCO_3$.

Scheme 1. Synthesis Route of the MGC and the Lithiation−Delithiation Processes

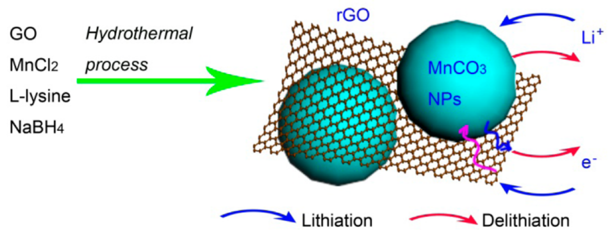

The microstructure of the MGC was observed in the TEM images (Figure 1). The shape of the rGO sheet remains in microscale. The $MnCO_3$ NPs are dispersed on the surface of the rGO sheets (Figure 1a and b). After an ultrasonic treatment, the $MnCO_3$ NPs are still anchored on the surface of the rGO sheets and no isolated $MnCO_3$ NPs can be found from the rGO sheets. The composite structure ensures the stability of the MGC in the used procedure. The lattice space of 0.283 nm is attributed to the crystalline plane (104) of $MnCO_3$, which provides further evidence for the existence of $MnCO_3$ NPs in the MGC (Figure 1c).[12,13] The diameter distribution of $MnCO_3$ NPs is mainly concentrated in the range 8−20 nm (Figure 1d). The diffraction rings and diffraction spots' multiple modes indicate the polycrystalline nature of the MGC (Figure S4). The AFM image and the corresponding section analysis suggest that the thickness of the rGO sheets (1.477 nm) and the height of the MGC (6.461 nm) are consistent with the results from TEM images (Figure 1e and f).

In the X-ray diffraction pattern, no clear peak can be found at 12.9°, which indicates that GO has been reduced to rGO sheets (Figure 2a).[14,15] The weak wide diffraction peak at ∼24.0° evidences that no aggregate rGO sheets formed and the rGO sheets possess a high degree of dispersion.[15] The diffraction peaks at 24.3° (*hkl*, 012), 31.5° (104), 37.7° (110), 41.5° (113), 45.3° (202), 49.8° (024), 51.8° (116), 60.3° (122), 63.9° (214), 68.0° (300), 72.4° (0012), 76.2° (0210), and 78.2° (128) match well with the standard pattern of $MnCO_3$

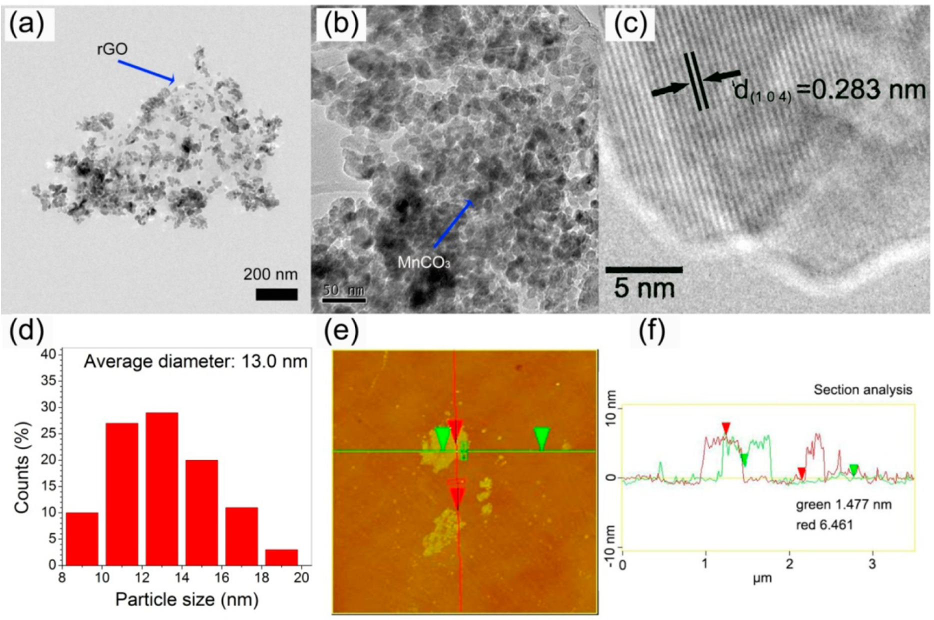

Figure 1. (a−c) TEM images with different magnification powers, (d) size distribution of $MnCO_3$ calculated from the TEM image, (e) AFM image, and (f) corresponding section analysis of the MGC.

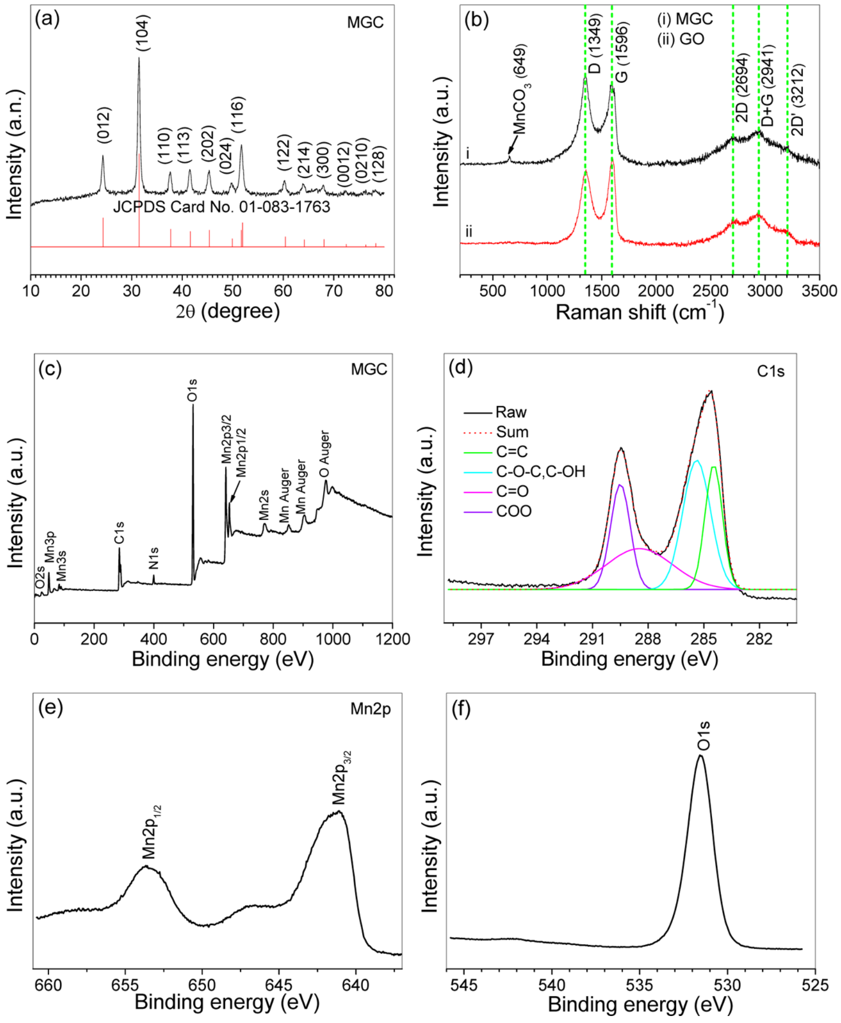

Figure 2. (a) XRD pattern of the MGC, (b) Raman spectra of GO and the MGC, (c) XPS survey spectrum of the MGC, and (d) corresponding fine spectra of C 1s, (e) Mn 2p, and (f) O 1s.

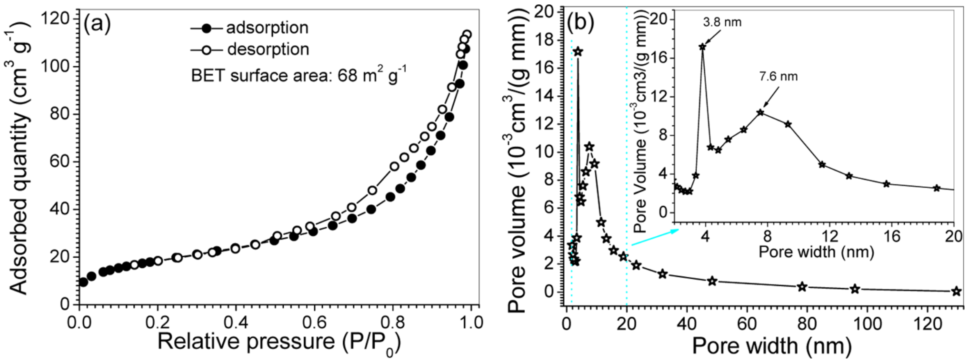

Figure 3. (a) N_2 adsorption (solid symbol) and desorption (open symbols) isotherms and (b) the pore size distribution of the MGC.

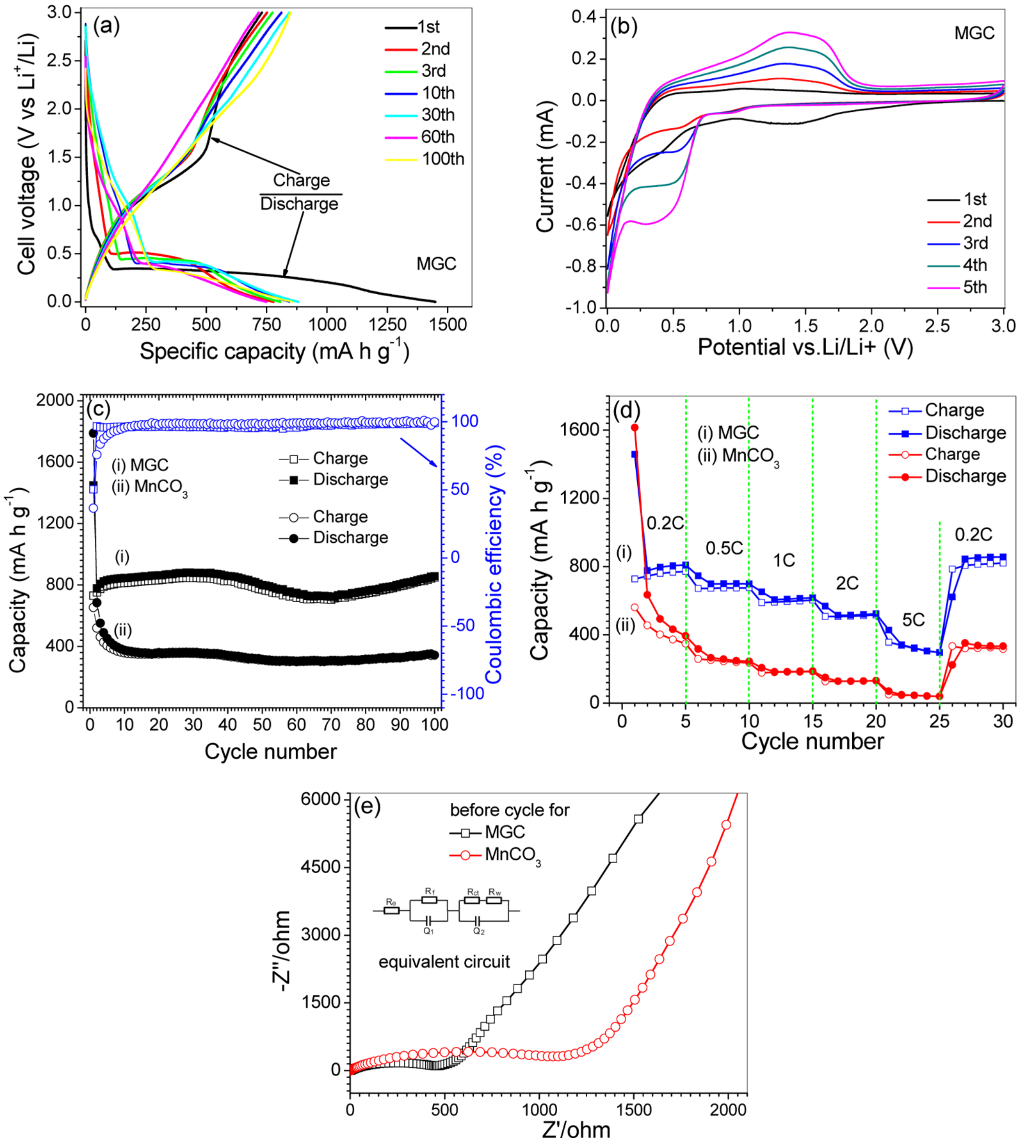

Figure 4. (a) Potential−capacity plot, (b) cyclic voltammogram curves, (c) cycling performance at 0.2 C, (d) cycling performance at various current rates, and (e) EIS spectra of commercial $MnCO_3$ and the MGC.

(JCPDS no. 83−1763).[16] The average crystallite size of $MnCO_3$ calculated with the Scherrer formula from the fwhm of the (104) plane is 15.2 nm, which is consistent with TEM analysis. The Raman shift at 649 cm^{-1} corresponds with the characteristic of $MnCO_3$ (Figure 2b).[17] The peaks at 1349 and 1596 cm^{-1} should be attributed to D and G mode vibrations of the rGO sheets, respectively.[15] The D peak of MGC (I_D/I_G = 1.11) increased compared to that of pure GO (I_D/I_G = 0.88). The composite interaction between $MnCO_3$ NPs and rGO sheets induced the decrease in the ordered degree of carbon atoms in rGO sheets. The decreasing G peak corresponding to the graphite domains in the rGO sheets also provides further evidence for the interaction in the composite material.[15] The wide and overlapped 2D (2694 cm^{-1}), D+G (2941 cm^{-1}), and 2D′ (3212 cm^{-1}) peaks show that the GO sheets possess multilayered structures. In the Raman spectra of MGC, the 2D, D+G, and 2D′ peaks become somewhat thin and separate due to the isolating effect of $MnCO_3$ NPs on the rGO sheets.

In the FT-IR spectra, the peak at 1630 cm^{-1} existing in the spectra of GO and MGC should be attributed to the stretching vibration of the C═C bond in graphite domains of the graphene sheets (Figure S5).[18] The peaks at 1464, 862, and 726 cm^{-1} correspond to the framework stretching vibration of $MnCO_3$.[19] The disappearance of the peak in the MGC at 1724 cm^{-1} attributed to C═O stretching of the carboxylic group[20] is present in the FT-IR spectrum of GO (Figure S5), indicating that the reduction of GO to rGO sheets in the MGC.

In the X-ray photoelectron spectra, the peaks of C 1s, Mn 2p, and O 1s electrons can be observed clearly, which display that the MGC includes C, Mn, and O elements (Figure 2c). In the fine structure of the C 1s spectrum treated by multiple-peak fitting, the main peak at 284.8 eV is attributed to carbon atoms in graphene domains of rGO (Figure 2d).[21] The secondary peak at 286.6 eV corresponds to carbon atoms connecting to hydroxyl and epoxide. The weak peak at 288.5 eV is induced by carbon atoms in the carbonate ions of residual ketone, which have been reduced in the MGC after the reduction process. It is known that the C−O bonds come from some defects including other oxygen atoms in the graphene sheets, which cannot be removed completely from the graphene sheets (here rGO sheets) by chemical reduction methods.[22,23] Thus, we can still find oxygen-related defects in the MGC by XPS analysis. The weak peak at 288.5 and 289.5 eV is induced by carbon atoms in carbonate ions of $MnCO_3$ NPs. The peaks at 641.2 and 653.6 eV corresponding to Mn^{2+} atoms in $MnCO_3$ NPs are consistent with other characterization results (Figure 2e). The binding energy peak at 531.5 eV can be attributed to the oxygen atoms from rGO and/or $MnCO_3$ (Figure 2f).

The surface area and porous structures of the MGC were evaluated by nitrogen adsorption−desorption at 77 K and are shown in Figure 3a. The isotherm of the MGC exhibited a type of *IV* curve that shows the presence of a mesopore and has a hysteresis loop at a relative pressure between 0.42 and 0.95, indicating pore size distributions in the mesoporous region. The BET surface area was 68 $\text{m}^2\cdot\text{g}^{-1}$. The pore size distributions in Figure 3b are narrowly in the range from 3 to 20 nm with two peak pore diameters of 3.8 and 7.6 nm.

MGC was used as anode active material to assemble a half-cell with Li platelets. The rate charging−discharging behaviors were investigated at various current rates (Figure 4a−c). According to the conversion of $MnCO_3$ to metal Mn and Li_2CO_3 (eq 1), the theoretic capacity of $MnCO_3$ is 467 $\text{mA}\cdot\text{h}\cdot\text{g}^{-1}$. The theoretic capacity of the MGC was calculated according to the following equation:

$$\begin{aligned} C_{\text{theoretical}} &= C_{MnCO_3} \times \text{mass percentage of } MnCO_3 \\ &\quad + C_{\text{Carbon}} \times \text{mass percentage of carbon} \\ &= 467 \times 68\% + 372 \times 32\% \\ &= 436\ \text{mA}\cdot\text{h}\cdot\text{g}^{-1} \end{aligned}$$

In the discharging process at 0.2 C (1 C = 600 $\text{mA}\cdot\text{h}\cdot\text{g}^{-1}$), a plateau in the range from 0.35 to 1.75 V can be observed and should be ascribed to the reduction lithiation process (Figure 4a).[21,24] The ramp under 0.35 V is due to the formation of $MnLi_x$ alloy. In the charging process, a plateau at 1.35 and 2.50 V is due to the oxidation delithiation and dealloying process.[25] The cyclic voltammogram curve of the MGC shows an oxidation peak in the range from 1.05 to 1.75 V, corresponding to the oxidation of Mn^0 metal in the first cycle (Figure 4b).[26] The reduction peak in the range from 0.35 to 0.55 V can be attributed to the reduction of $MnCO_3$ NPs to Mn^0.[26,27] The oxidation and reduction peaks correspond to the delithiation and lithiation processes, which is consistent with the rate charging−discharging curves. The CV curve of the second cycle is similar to that for the first cycle, suggesting that reduction and oxidation of the MGC is a reversible process (eq 1). The symmetry of CV curve also is evidence for the reversible reaction of the MGC.[28] The oxidation peaks of the MGC shift left and the reduction peak shifts right compared to that of pristine $MnCO_3$ NPs. The total cell reaction should be as follows:

$$MnCO_3 + 2Li \leftrightarrow Mn^0 + Li_2CO_3 \qquad (1)$$

$$Mn + xLi \leftrightarrow MnLi_x \qquad (2)$$

At 0.2 C, an initial discharging specific capacity of 1450 $\text{mA}\cdot\text{h}\cdot\text{g}^{-1}$ was obtained (Figure 4c). The excess capacity should partially be due to the irreversible formation of a solid electrolyte layer (SEI). In the second cycle, the capacity reduced to 780 $\text{mA}\cdot\text{h}\cdot\text{g}^{-1}$ and then increased up to 830 $\text{mA}\cdot\text{h}\cdot\text{g}^{-1}$ in the fifth cycle. It is mentioned that the average capacity remained at a high level of 709, 620, and 528 $\text{mA}\cdot\text{h}\cdot\text{g}^{-1}$ with a current rate of 0.5, 1.0, and 2.0 C, respectively. Even at 5.0 C, a slight decrease of the capacity to 339 $\text{mA}\cdot\text{h}\cdot\text{g}^{-1}$ still remains (Figure 4d). It should be concluded that the MGC possesses excellent current rate tolerance under 2.0 C. Is should be pointed out that the charging−discharging performances were performed after rate charging−discharging cycles. At a recovered rate of 0.2 C, a high capacity up to 845 $\text{mA}\cdot\text{h}\cdot\text{g}^{-1}$ was obtained and kept. These high capacities and the increasing Coulombic efficiency suggest that the MGC possesses a superior recyclability. The half-cell also provided excellent cycling performances at a constant current rate of 0.2 C. The capacity reached 780 $\text{mA}\cdot\text{h}\cdot\text{g}^{-1}$ and was maintained at 857 $\text{mA}\cdot\text{h}\cdot\text{g}^{-1}$ (197% of theoretic capacity) after 100 cycles (Figure 4c). The excess capacity compared to the calculated theoretic capacity (436 $\text{mA}\cdot\text{h}\cdot\text{g}^{-1}$) should be attributed mainly to the reversible formation of a $MnLi_x$ alloy phase (eq 2), the exfoliation of graphene sheets, and the pseudocapacitance of the electrode material.[29] Pristine $MnCO_3$ (Figure S1) as active material exhibited a somewhat lower specific capacity, a poor current rate performance, and fair recyclability at various current rates (Figure 4c and d). The serious structure and volume change of $MnCO_3$ NPs in the charging−discharging process was buffered effectively by the existence of rGO sheets in the MGC, which prevents serious capacity fading.[30]

The electrochemical impedance spectra displayed a smaller half-cycle curve and lower slope of the straight line for the MGC compared to those for pristine $MnCO_3$ (Figure 4e). This should be derived from the improved electron conductivity and ion mobility of the MGC.[31] The existence of rGO is vital for the improvement in the electron conductivity in the MGC.[32] After being cycled three times, similar CV curves were obtained and showed the highly reversible property of the MGC in LIBs (Figure S6). The dispersed $MnCO_3$ NPs on rGO nanosheets improved the accessibility of the MGC.[16] The assembly of rGO sheets and $MnCO_3$ NPs forms a porous structure and facilitates the penetration of electrolyte into the electrode of LIBs.[33] These structure factors are responsible for the superior electrochemical properties of the MGC in LIBs.[34]

Aragon and co-workers[24] reported that $MnCO_3$ presents a good electrochemical performance. However, they did not mention the value of the defined 1C in their paper. Also they just provided the measurement of 25 cycles for the discharge/charge processes. By the way, $MnCO_3$ presents a specific capacity of 450 $mA \cdot h \cdot g^{-1}$ at the 25th cycle and ca. 400 $mA \cdot h \cdot g^{-1}$ measured under the 2 C condition, while our MGC presents 709, 620, and 528 $mA \cdot h \cdot g^{-1}$ with a current rate of 0.5, 1.0, and 2.0 C, respectively. It is worthy to mention that the capacity can reach 780 $mA \cdot h \cdot g^{-1}$ and stay at 857 $mA \cdot h \cdot g^{-1}$. Thus, our MGC presents even better electrochemical behavior with a higher capacity and excellent cycling stability, which is attributed to the hybrid structure of the MGC and its good conductivity. The latter has been demonstrated by the electrochemical impedance spectra (Figure 4e).

4. CONCLUSIONS

In conclusion, the MGC has been fabricated by a hydrothermal synthesis method of $MnCO_3$ NPs coordinating with the reduction process of GO. $MnCO_3$ NPs are anchored onto the surface of rGO sheets. No high-temperature treatment is needed in the preparation process. With the MGC as an anode active material for LIBs, high specific capacities up to 857 $mA \cdot h \cdot g^{-1}$ can be obtained after 100 cycles. The various current rates from 0.2 to 5.0 C do not exhibit a negative effect on the recycling stability of the MGC. The assembly and interaction between the layer structure of rGO and $MnCO_3$ NPs warrant high structure stability and accessibility of the MGC. This MGC and solution-process synthesis will find potential applications in the design of novel functional materials and LIBs.

■ ASSOCIATED CONTENT

Ⓢ Supporting Information

Selected area electron diffraction, FTIR spectra, and CV plot of the MGC and XRD pattern and TEM images of the as-synthesized so-called $MnCO_3$ containing a Mn_3O_4 impurity. This material is available free of charge via the Internet at http://pubs.acs.org.

■ AUTHOR INFORMATION

Corresponding Authors

*E-mail: kongxh@ustb.edu.cn.
*E-mail: hqcao@tsinghua.edu.cn.

Notes

The authors declare no competing financial interest.

■ ACKNOWLEDGMENTS

Financial support from the 973 Program (2013CB933804), the National Natural Science Foundation of China (21271112, 21231005), the Innovation Program of Shanghai Municipal Education Commission (No. 13ZZ071), and Shanghai University Innovation Foundation is acknowledged.

■ REFERENCES

(1) Kang, B.; Ceder, G. *Nature* **2009**, *458*, 190−193.

(2) Reddy, M. V.; SubbaRao, G. V.; Chowdari, B. V. R. *Chem. Rev.* **2013**, *113*, 5364−5457.

(3) Koo, B.; Xiong, H.; Slater, M. D.; Prakapenka, V. B.; Balasubramanian, M.; Podsiadlo, P.; Johnson, C. S.; Rajh, T.; Shevchenko, E. V. *Nano Lett.* **2012**, *12*, 2429−2435.

(4) Gong, Y. J.; Yang, S. B.; Liu, Z.; Ma, L. L.; Vajtai, R.; Ajayan, P. M. *Adv. Mater.* **2013**, *25*, 3979−3984.

(5) Dunn, B.; Kamath, H.; Tarascon, J. M. *Science* **2011**, *334*, 928−935.

(6) Wang, H. L.; Yang, Y.; Liang, Y. Y.; Cui, L. F.; Casalongue, H. S.; Li, Y. G.; Hong, G. S.; Cui, Y.; Dai, H. J. *Angew. Chem., Int. Ed.* **2011**, *50*, 7364−7368.

(7) Li, B. J.; Cao, H. Q.; Shao, J.; Qu, M. Z. *Chem. Commun.* **2011**, *47*, 10374−10376.

(8) Luo, J. S.; Liu, J. L.; Zeng, Z. Y.; Ng, C. F.; Ma, L. J.; Zhang, H.; Lin, J. Y.; Shen, Z. X.; Fan, H. J. *Nano Lett.* **2013**, *13*, 6136−6143.

(9) Yang, Y.; Fan, X. J.; Casillas, G.; Peng, Z. W.; Ruan, G. D.; Wang, G.; Yacaman, M. J.; Tour, J. M. *ACS Nano* **2014**, *8*, 3939−3946.

(10) Wang, H. L.; Cui, L. F.; Yang, Y.; Casalongue, H. S.; Robinson, J. T.; Liang, Y. Y.; Cui, Y.; Dai, H. J. *J. Am. Chem. Soc.* **2010**, *132*, 13978−13980.

(11) Li, B. J.; Cao, H. Q.; Shao, J.; Qu, M. Z.; Warner, J. H. *J. Mater. Chem.* **2011**, *21*, 5069−5075.

(12) Duan, X. C.; Lian, J. B.; Ma, J. M.; Kim, T.; Zheng, W. J. *Cryst. Growth Des.* **2010**, *10*, 4449−4455.

(13) Duan, X. C.; Ma, J. M.; Lian, J. B.; Kim, T.; Zheng, W. J. *Chem. Commun.* **2010**, *46*, 7133−7135.

(14) Guo, C. X.; Yang, H. B.; Sheng, Z. M.; Lu, Z. S.; Song, Q. L.; Li, C. M. *Angew. Chem., Int. Ed.* **2010**, *49*, 3014−3017.

(15) Zhou, Q.; Zhao, Z. B.; Wang, Z. Y.; Dong, Y. F.; Wang, X. Z.; Gogotsi, Y.; Qiu, J. S. *Nanoscale* **2014**, *6*, 2286−2291.

(16) Lee, H. K.; Sakemi, D.; Selyanchyn, R.; Lee, C. G.; Lee, S. W. *ACS Appl. Mater. Interfaces* **2014**, *6*, 57−64.

(17) Yuan, J. J.; Zheng, Y.; Chen, S.; Tang, Y. H.; Jaroniec, M.; Qiao, S. Z. *Chem. Commun.* **2013**, *49*, 7705−7707.

(18) Yin, J. F.; Cao, H. Q.; Zhou, Z. F.; Zhang, J. X.; Qu, M. Z. *J. Mater. Chem.* **2012**, *22*, 23963−23970.

(19) Wang, L. Z.; Tang, F. Q.; Ozawa, K.; Chen, Z. G.; Mukherj, A.; Zhu, Y. C.; Zou, J.; Cheng, H. M.; Lu, G. Q. *Angew. Chem., Int. Ed.* **2009**, *48*, 7048−7051.

(20) Liang, Y.; Wu, D.; Feng, X.; Müllen, K. *Adv. Mater.* **2009**, *21*, 1679−1683.

(21) Zhang, F.; Cao, H. Q.; Yue, D. M.; Zhang, J. X.; Qu, M. Z. *Inorg. Chem.* **2012**, *51*, 9544−9551.

(22) Wang, H. L.; Robinson, T.; Li, X. L.; Dai, H. J. *J. Am. Chem. Soc.* **2008**, *131*, 9910−9911.

(23) Li, X. L.; Zhang, G. Y.; Bai, X. D.; Sun, X. M.; Wang, X. R.; Wang, E. G.; Dai, H. J. *Nat. Nanotechnol.* **2008**, *3*, 538−542.

(24) Aragón, M. J.; León, B.; Vicente, C. P.; Tirado, J. L. *J. Power Sources* **2011**, *196*, 2863−2866.

(25) Aragón, M. J.; Vicente, C. P.; Tirado, J. L. *Electrochem. Commun.* **2007**, *9*, 1744−1748.

(26) Mirhashemihaghighi, S.; León, B.; Vicente, C. P.; Tirado, J. L.; Stoyanova, R.; Yoncheva, M.; Zhecheva, E.; Puche, R. S.; Arroyo, E. M.; Paz, J. R. *Inorg. Chem.* **2012**, *51*, 5554−5560.

(27) Sharma, Y.; Sharma, N.; Rao, G. V. S.; Chowdari, B. V. R. *J. Mater. Chem.* **2009**, *19*, 5047−5054.

(28) Shao, L. Y.; Shu, J.; Ma, R.; Shui, M.; Hou, L.; Wu, K. Q.; Wang, D. J.; Ren, Y. L. *Int. J. Electrochem. Sci.* **2013**, *8*, 1170−1180.

(29) Zhang, K. J.; Han, P. X.; Gu, L.; Zhang, L. X.; Liu, Z. H.; Kong, Q. S.; Zhang, C. J.; Dong, S. M.; Zhang, Z. Y.; Yao, J. H.; Xu, H. X.; Cui, G. L.; Chen, L. Q. *ACS Appl. Mater. Interfaces* **2012**, *4*, 658−664.

(30) Wang, B.; Li, X. L.; Zhang, X. F.; Luo, B.; Jin, M. H.; Liang, M. H.; Dayeh, S. A.; Picraux, S. T.; Zhi, L. J. *ACS Nano* **2013**, *7*, 1437−1445.

(31) Zhu, J. X.; Zhu, T.; Zhou, X. Z.; Zhang, Y. Y.; Lou, X. L.; Chen, X. D.; Zhang, H.; Hng, H. H.; Yan, Q. Y. *Nanoscale* **2011**, *3*, 1084−1089.

(32) Jiang, K. C.; Xin, S.; Lee, J. S.; Kim, J.; Xiao, X. L.; Guo, Y. G. *Phys. Chem. Chem. Phys.* **2012**, *14*, 2934−2939.

(33) Kim, I. Y.; Lee, J. M.; Kim, T. W.; Kim, H. N.; Kim, H. I.; Choi, W.; Hwang, S. J. *Small* **2012**, *8*, 1038−1048.

(34) Gwon, H.; Hong, J.; Kim, H.; Seo, D. H.; Jeon, S.; Kang, K. *Energy Environ. Sci.* **2014**, *7*, 538−551.